03/04/22

Targeting One- and Two-dimensional Ta-Te Structures via Nanotube Encapsulation

Scott Stonemeyer[1,2,3,4,‡], Mehmet Dogan[1,3,‡], Jeffrey D. Cain[1,3,4], Amin Azizi[1,4], Derek C. Popple[1,2,3,4], Austin Culp[1], Chengyu Song[5], Peter Ercius[5], Marvin L. Cohen[1,3], and Alex Zettl[1,3,4*]

[1]*Department of Physics, University of California at Berkeley, Berkeley, CA 94720, USA*

[2]*Department of Chemistry, University of California at Berkeley, Berkeley, CA 94720, USA*

[3]*Materials Sciences Division, Lawrence Berkeley National Laboratory, Berkeley, CA 94720, USA*

[4]*Kavli Energy NanoSciences Institute at the University of California at Berkeley, Berkeley, CA 94720, USA*

[5]*National Center for Electron Microscopy, The Molecular Foundry, Lawrence Berkeley National Laboratory, Berkeley, CA 94720 USA*

[‡]These authors contributed equally

*e-mail: azettl@berkeley.edu

ABSTRACT

Fine control over material synthesis on the nanoscale can facilitate the stabilization of competing crystalline structures. Here we demonstrate how carbon nanotube reaction vessels can be used to selectively create one-dimensional $TaTe_3$ chains or two-dimensional $TaTe_2$ nanoribbons with exquisite control of the chain number or nanoribbon thickness and width. Transmission electron microscopy and scanning transmission electron microscopy reveal the detailed atomic structure of the encapsulated materials. Complex superstructures such as multi-

chain spiraling and apparent multi-layer moirés are observed. The rare 2H phase of $TaTe_2$ (1H in monolayer) is found to be abundant as an encapsulated nanoribbon inside carbon nanotubes. The experimental results are complemented by density functional theory calculations for the atomic and electronic structure, which uncovers the prevalence of 2H-$TaTe_2$ due to nanotube-to-nanoribbon charge transfer and size confinement. Calculations also reveal new 1T' type charge density wave phases in $TaTe_2$ that could be observed in experimental studies.

Keywords: One-dimensional materials, two-dimensional materials, nanoribbons, transition metal dichalcogenides, scanning transmission electron microscopy, nanotubes

1. INTRODUCTION

Isolating specific stoichiometries and structures of materials is a key goal of material property design and control. Transition metal chalcogenides of the form MX_n, with M a transition metal, X a chalcogen, and n typically an integer, are enjoying a resurgence in popularity for fundamental science study and applications including field-effect transistors, photodetectors, catalysts, and optoelectronics. [1–7] The materials can assume an abundance of different stoichiometries and structures, but two of the more popular configurations are the transition metal dichalcogenides (TMDs), with n = 2, and the transition metal trichalcogenides (TMTs), with n = 3. TMTs are typically chain-like exhibiting quasi-one-dimensional physical and electronic structure, while TMDs are typically sheet-like with quasi-two-dimensional structure.

Many M-X combinations readily adopt independently the TMD and TMT stoichiometry, as exemplified by the well-known compounds TiS_2 and TiS_3, $NbSe_2$ and $NbSe_3$, and $HfTe_2$ and $HfTe_3$. For these materials, obtaining a specific stoichiometry, i.e. selecting either TMD or TMT, is easily achieved by adjusting the reaction temperature and stoichiometric loading of reagents. [8–10] On the other hand, some M-X combinations are not so easily separated into TMD or TMT, as is the case for tantalum telluride (Ta-Te). Scant previous reports comment on the overall crystalline structure of $TaTe_n$ compounds, alluding to the fact that they are low-dimensional structures similar to other members of the TMD and TMT family, but difficulty in isolating specific phases from the Ta-Te system via temperature or precursor loading has prevented significant further study. [9,11]

Recent developments in MX_n stabilization and isolation via nanotube encapsulation demonstrate that a physically-confining carbon nanotube (CNT) or boron nitride nanotube

(BNNT) “reaction vessel” affords an addition powerful synthesis control parameter for the selection of a specific stoichiometry. [12,13] Indeed, the method has allowed for the stabilization of previously unknown MX_n stoichiometries and crystal structures, [14–18] leading to novel electrical and optical properties. [19,20]

Here, we report the successful targeted isolation of $TaTe_3$ and $TaTe_2$ via CNT encapsulation. The specific stoichiometry can be preferentially selected by choosing the proper nanotube inner diameter and overall reaction temperature of the synthesis. Encapsulation provides not only greater experimental control over the obtained structure, but, once the materials are formed, it facilitates further characterization without the deleterious effects of rapid oxidation. We find not only excellent reproducibility for creating “expected” phases of $TaTe_n$ (including TMT chain spiraling), but the method yields intriguing and completely new Ta-Te configurations, such as a moiré-interference-like structure whose detailed atomic configuration has yet to be determined. We complement our experimental studies with first-principles theoretical calculations to reveal the electronic structure of the newly isolated $TaTe_3$ and $TaTe_2$ phases, and to gain further insight into confinement size-effects on the electronic structure of TMD materials generally.

2. SYNTHESIS

Truncating 2-D TMD materials at low layer number, and 1-D TMT materials to low chain number, via nanotube encapsulation is facilitated by the inherent hierarchical crystal structure. Figs. 1 and 2 present calculated atomic structures of the $TaTe_3$ and $TaTe_2$ species, respectively, highlighting the vdW nature of the crystalline materials. The weak vdW structure of the crystal allows for isolation within the CNT of the 2-D sheets as few-layer or monolayer

nanoribbons (NRs), and 1-D chains down to few-chains or the single-chain limit. The encapsulation can also stabilize some crystal structures that are inherently unstable in bulk form (and have thus previously not been successfully synthesized).

Encapsulated $TaTe_2$ NRs, $TaTe_3$ chains, and $TaTe_y$ moiré-like structures are synthesized within CNTs using a procedure similar to that used previously for the growth of confined TaS_2, $NbSe_3$, and $HfTe_3$. [15,18,21] For $TaTe_2$ and $TaTe_3$, stoichiometric quantities of Ta powder and Te shot (~450mg total), 1-2mg of opened multi-walled CNTs with inner diameter ranging from 1.0 to 10.0 nm (CheapTubes, 90% SW-DW CNT), and ~5mg/cm^3 (ampoule volume) of I_2 are sealed under vacuum (~10^{-6} Torr) in a quartz ampoule. The $TaTe_y$ moiré structures can be synthesized following the stoichiometry and loading of $TaTe_2$. The ampoule is heated in a single-zone furnace at 600-900ºC for 3 days, then cooled to room temperature over 1-5 days.

Selectively synthesizing the TMT form of $TaTe_n$, i.e.$TaTe_3$, is achieved by using an overall reaction temperature near 600ºC. Selecting the TMD form, i.e. $TaTe_2$, is achieved through higher reaction temperatures, ranging from 800-900ºC, along with the moiré $TaTe_y$ structure.

3. STRUCTURAL CHARACTERIZATION

Ta-Te filled CNTs are dispersed in isopropyl alcohol by bath sonication for 1 hour and drop-cast onto lacey grids for transmission electron microscopy (TEM) and scanning transmission electron microscopy (STEM) imaging. TEM imaging is carried out on a JEOL 2010 microscope operated at 80 keV.STEM is carried out on the TEAM 0.5 microscope, a Titan 80-300 with an ultra-twin pole piece gap, DCOR probe aberration corrector, and is operated at 80

kV with semi-convergence angle of 30 mrad. STEM images are acquired using the ADF-STEM detector with an inner angle of 60 mrad and a beam current of approximately 70 pA.

$TaTe_3$ TMTs

Fig. 1 presents selected TEM and STEM images for synthesized TMT $TaTe_3$. Fig. 1a shows a multi-chain specimen encapsulated within a 9.4 nm inner diameter CNT. The lattice constants for bulk $TaTe_3$ have not been previously established to the best of our knowledge. In Figs. 1d,e, we present computationally optimized structures for bulk $TaTe_3$ which has the Te atoms oriented in isosceles triangles perpendicular to the chain direction. The lattice constants along the *a*, *b* and *c* directions are 3.72, 10.93, and 17.04 Å, respectively. Strong intrachain bonding is observed along the *a*-axis, while van der Waals gaps can be seen between the chains. These values are consistent with our experimental TEM and STEM observations. We have found this 24-atom phase by running a randomized search in unit cells with 4–48 atoms. In addition to being the configuration with the lowest energy, it is also dynamically stable, as presented in Fig. S1a. We have computed this phonon spectrum using a 3×2×1 (144-atom) supercell *via* the frozen phonon method.

In other nanotube-encapsulated MX_3 systems, the trigonal prismatic chains often exhibit new structural configurations, such as on-chain torsional distortions or multi-chain spiraling. [15,18] As shown in Figs. 1b,c, we observe similar few-chain spiraling behavior for $TaTe_3$ encapsulated within a 2.2 nm and 2.6 nm inner diameter CNT, respectively. In Fig. 1f, we present the theoretically relaxed atomic structure of single-chain $TaTe_3$, which adopts a geometry with equilateral triangles of Te atoms perpendicular to the chain direction with a periodicity of 3 $TaTe_3$ units and a lattice constant of 8.54 Å. The electronic band structures, including spin-orbit

coupling, for bulk and single chain $TaTe_3$ are presented in Figs. 1g,h, and exhibit metallic behavior. The 3-unit single chain structure is dynamically stable as shown in Fig. S1b. To compare it with structures with different periodicities, we have run calculations with 1 to 6 $TaTe_3$ units in a cell, which all have higher energy than the 3-unit structure (Fig. S1c). The atomic and electronic structure of these configurations are presented in Fig. S2.

$TaTe_2$ TMDs

Encapsulated $TaTe_2$ manifests itself as nanoribbons (NRs), where the width of the ribbon often just spans the inner diameter of the encapsulating CNT. The NRs can be composed of very few layers, most often as monolayers or bilayers. Similar behavior has been observed for other MX_2 encapsulated NRs. [21,22] We note that at the elevated TMD reaction temperatures, no concomitant TMT specimens are observed, indicating that the encapsulation, coupled with higher temperatures, strongly favors the dichalcogenide phase of the TaTe system.

Fig. 2 shows encapsulated $TaTe_2$ NRs in various projections. Fig. 2a shows a 7.4 nm wide bilayer NR, which interestingly and somewhat unusually, begins to fold in on itself (curl) at the edges due to the extreme confinement. Figs. 2b,c,d are examples of 5.0 nm, 4.8 nm, and 6.4 nm wide monolayer NR specimens, respectively. A closer look at these STEM images reveals that these NRs adopt the 2H phase in the monolayer, also called 1H (as highlighted in Fig. 2c), so, for simplicity and clarity the 2H phase is used as modeling in the side and plan view atomic models in Figs. 2e,f. The curling observed in the multilayer specimen precludes the current study from assigning a polytype to the multilayer encapsulated NR. However, the energy differences between 1H-based polytypes (*e.g.* 2H *vs.* 3R) is expected to be of the order of 0.01 eV [23], much smaller than the energy difference between 2H and 1T′ (>0.1 eV, as discussed below

below), so we continue the use of the 2H phase observed in the monolayer for atomic modeling of 1H-based multilayer $TaTe_2$.

Ta-Te Moiré-like Structures

In conjunction with TMD NRs observed at higher reaction temperatures, we find some unexpected, yet fascinating structures stabilized within the CNT. The structure is not only stabilized in an encapsulated form, but highly reproducible and transferrable to varying pattern widths. The patterns are moiré-like in appearance as observed in the projection plane. Fig. 3 illustrates several examples of the moiré-like structure observed. Fig. 3a shows a TEM image of a moiré-like structure roughly 3 patterns wide. Specimen ranging from a single pattern wide up to five patterns wide can be found in the sample, with the moiré-type pattern retaining the same overall structure and spacing. Figs. 3b,c,d each show the encapsulated moiré structure in increasing widths, from a single, double, and triple pattern wide, respectively. The corresponding widths of these structures are 2.6 nm, 3.1 nm, and 3.6 nm, respectively, indicating the moiré-like structure itself is roughly 0.5 nm in width and grows in a quantized fashion, requiring select CNTs of specific widths for each successive pattern added widthwise. Initial studies of these encapsulated patterned structures in previous work indicates these encapsulated structures are likely a core-shell entity. [24] This type of extended, coherent structure has not been observed in any highly confined material systems before. However, similar coherent structural patterns have been observed in layered TMD material systems, indicating these moiré-type structures could also arise from stacked layers of $TaTe_2$ inside of the CNT or a chiral TMD nanotube. [25] However, further investigation is required to elucidate the underlying atomic, and electronic structures of these moiré-like species.

4. DISCUSSION

The fact that the 2H (or 1H for monolayer) phase is experimentally observed for $TaTe_2$ NRs encapsulated in CNTs is unexpected, since $TaTe_2$ in bulk crystalline form is normally observed and reported in a distorted 1T phase (1T′) that is obtained by a 3×1 reconstruction of the 1T phase. [26–29] The only other experimental evidence of 2H-$TaTe_2$ that we are aware of is for a monolayer (1H) on bulk 1T′-$TaTe_2$. [30] The rarity of the 2H phase is consistent with the fact that it is 0.106 (0.147) eV/$TaTe_2$ higher in total energy than the 1T′ in monolayer (bulk), as demonstrated in Fig. 4a.

In order to investigate the potential mechanisms that lead to the stabilization of the 2H phase, we have conducted a series of DFT relaxations. To start with, the optimized configurations of the 1T, 1H and 1T′ monolayers are obtained, which are presented in Fig. S1a,b,c, respectively, along with their corresponding band structures that include the spin–orbit interaction. We find that the 1H monolayer is virtually degenerate with the 1T monolayer, whereas the 1T′ monolayer is 106 meV/$TaTe_2$ unit lower in energy than the 1T phase, which is in agreement with previous calculations. [31] The lattice parameter for the 1T and 1H phases are calculated as 3.69 and 3.67 Å, respectively, and for 1T′, we find $a=10.94$ Å, $b=3.46$ Å and $\gamma=61.7$ °. The atomic and electronic structures of these phases are presented in Fig. S3. In the bulk limit, we find the interlayer distance for the 1T, 2H and 1T′ phases to be 6.77, 6.88 and 6.64 Å, respectively.

The energetics of nanoribbons are expected to differ from the energetics of infinite layers. In order to explore these differences, we must first calculate the optimal configurations of $TaTe_2$ NRs in the three phases (1H, 1T, and 1T') from 5- to 12-unit cells (u.c.) wide. We have limited

these calculations to zigzag NRs, as zig-zag edges are experimentally observed in the STEM images in Fig. 2. In constructing nanoribbons, considerations about the NR axis chosen and termination need to be made. In the lower symmetry 1T′ phase, because the *a* and the *b* directions are inequivalent, repeating along either direction yields different NR geometries (Fig. S4c vs. Fig. S4d-f). Also, if the structure is repeated along the *b* direction, three NR geometries are possible for each width (Fig. S4d-f). In addition to the NR axis chosen, various edge terminations are possible for each phase. For simplicity, we choose to keep the NRs stoichiometric, *i.e.*, the Te:Ta ratio remains 2:1. For stoichiometric NRs, in the case of the 1H phase, the natural choice is to terminate one edge with Ta and the other edge with Te_2 (Fig. S4b). In the 1T and 1T′ cases, lowest energies are obtained when both edges are terminated with Te_1 (Fig. S4a and S4c-f). We have compared this termination scheme to one where one edge is terminated with Ta and the other with Te_2, to find that it leads to energies that are a few tenths of an eV/$TaTe_2$ unit higher in energy for each NR. We present the relaxed, 6 u.c. wide NRs of all configurations of monolayer $TaTe_2$ in Fig. S4.

We examine the energetics of these 6 different NR configurations in Fig. 4b, with the 1T NR energy set to zero. From Fig. 4a and 4b, we find that, when only taking geometry and size into consideration, the NR favors the 1T phase in terms of its relative position in energy with respect to the other two phases. This is likely because the distortion of the atomic coordinates in 1T is smaller and more localized to the edges. In contrast, the 1H phase becomes disfavored as a NR, likely because of the more drastic distortions that occur especially at the Ta edge. We point out that in the limit of NR width going to infinity, the data points in Fig. 4b should approach the leftmost data points in Fig. 4a, and this trend does not visibly begin by the largest width we have considered. Thus, it is safe to say that the 1H phase will remain disfavored for the even wider

NRs that are observed in the experiment. Therefore, NR edge effects and size alone cannot explain the favorability of the 1H phase experimentally observed in the carbon nanotubes, so we must examine other phenomena known to exist in encapsulated species, such as charge transfer.

When studying the energetics of charge transfer, it is important to notice the differences in the band structures of the 1H phase and the other two phases, as shown in Fig. S1. As more electrons are added to the system, the tops of the valence bands that cross the Fermi energy in the 1H phase are filled. Such a large density of low energy states is not available for the 1T and 1T′ phases. To check the effect of added charge on energetics, we have relaxed the three phases in 3×3 phases and added integer numbers of electrons. The resulting energy *vs.* charge graph is presented in Fig. 4c, which shows that the 1H phase is indeed favored in the electron rich environment and becomes the ground state when the system has an extra third of an electron per formula unit. Hence, if encapsulation by CNTs provides this electron rich environment, then the 1H phase NR is energetically preferred over the more commonly reported bulk 1T′ phase.

In previous studies, encapsulated TMTs were found to gain electrons from the CNTs. [18,32] To investigate the same possibility for TMD NRs, we have generated model $TaTe_2$–CNT systems where the armchair CNTs are constrained the lattice constant of $TaTe_2$ NRs. We have taken 5, 6 and 7 u.c. wide nanoribbons and armchair CNTs with $m=n=16,17,18,\wedge 19$. Because the lattice constant of these CNTs, *i.e.* 2.46 Å, is approximately two thirds of the NR lattice constants, we have created simulation cells with 3 u.c. of CNT and 2 u.c. of $TaTe_2$ NRs. This has led to a total of 32 calculations with 222 to 270 atoms. To avoid even larger calculations, we have omitted 1T′ (a) NRs and only included 1T′ (b-1,2,3) NRs. To approximate the effect of compressive strain on CNTs, which are 0.9%, 0.5% and 6.3% for 1T, 1H and 1T′ NRs, respectively, we have increased their diameter proportionally, assuming a

Poisson ratio of 0.2 based on the existing literature. [33–38] To estimate the charge transfer between the CNTs and the NRs, we have simply calculated the electronic structure of these systems without attempting atomic relaxation. However, the results are instructive in terms of energetics as well. In Fig. 4d, we plot the binding energy of each configuration as a function of the distance between the NR edge and the CNT. Here, the binding energy is defined as the total energy of the CNT+NR system minus the total energies of the CNT and NR systems separately, and can be negative (attractive) or positive (repulsive). The NR–CNT distance is defined as half of the difference between the diameter of the CNT and the width of the NR. We find that the system is stable in this sense when the NR–CNT distance is 3 Å or larger. We also find that the in the optimal 3 to 4 Å range, the 1H phase lies about 0.5 eV/f.u. lower in energy than the other phases. Thus, encapsulation alone favors the 1H phase NRs.

Finally, we have computed the charge transfer between the CNT and the NR in each case using the charge redistribution defined as $\Delta\rho(r,\phi,x)=\rho(\text{CNT+NR})-\rho(\text{CNT})-\rho(\text{NR})$, where the $\Delta\rho$ is expressed in terms of cylindrical coordinates with x being the coordinate along the periodic direction. Two examples of $\Delta\rho$ can be seen in Fig. S5, which shows that the electron transfer occurs from the CNT to the NR, which is the case for all the calculations. To get the exact value of the electron transfer, Δq, we have plotted $\int_0^{2\pi}\int_0^{a} r\,\Delta\rho(r,\phi,x)\,dx d\phi$ as a function of r (where a is the lattice parameter) and integrated the result up to the value of r at which the integral changes sign. For the structures with a binding energy of 1 eV or less, we have found Δq to be in the range of 0.14 to 0.27 e per $TaTe_2$. This range of electron transfer falls short of the 1/3 e per $TaTe_2$ calculated for the favorability of the 1H phase, however the 1/3 e per $TaTe_2$ is for

an infinite layer. An electron transfer of 0.27 *e* per $TaTe_2$ falls roughly where the energetic favorability of the 1H and 1T'phase (in Fig. 7c) are roughly equal. Therefore, the electron transfer combined with the favorability of the 1H phase NRs given the preferred NR–CNT distance of 3-4 Å (Fig. 4d), suffice to explain the abundance of 1H NRs observed in our experiments.

In our calculations on $TaTe_2$ monolayers, we have also discovered new 1T′-type charge density wave (CDW) phases, which are presented in Fig. S6 along with the already known phases. We have found these phases by applying distortions similar to the one that produces the 3×1 1T′ phase from the 1T phase along both lattice directions. To confirm that these structures are dynamically stable, we have perturbed their atomic coordinates by random fractions of 0.2 Å in 6×6 unit cells and re-relaxed them (3 times each). To the best of our knowledge, the configurations shown in Fig. S6d-f have not been reported before (the 3×3 structure found in ref. [31] has a different geometry). It is important to note that 3×3 CDW distortions have been observed in $TaTe_2$ experimentally, along with several other periodicities, so there is a need for computational work to pin down the exact atomic configurations of such phases. [27–29] The electronic structures of these phases are presented in Fig. S6, which demonstrate that the system reduces the density of states at the Fermi energy by allowing distortions in larger unit cells (or distortions with smaller *q*).

5. CONCLUSION

The TaTe system demonstrates significant material flexibility yet specificity in the encapsulation study presented above. Successful targeted synthesis of both $TaTe_3$ and $TaTe_2$ via encapsulation with CNT is discussed in detail, with the specific stoichiometry of the TaTe

system grown in the confined space within the CNT preferentially selected via the reaction temperature. Surprisingly, an unexpected 2H phase of the $TaTe_2$ NR is experimentally observed (1H in monolayer). DFT calculations uncover contributions of charge transfer and proximity of the encapsulated species to the CNT to alter the energetics of the $TaTe_2$ phases, accounting for the stability of the 2H phase as an encapsulated species. A new patterned structure exhibiting unique and fascinating moiré-like features is presented. Additional studies and examination of the unique patterned structure is required to elucidate the underlaying atomic and electronic structure. However, the control shown in the encapsulated $TaTe_x$ systems coupled with the unique structure and strong dependence of phase energetics as a function of size and energy transfer, further pushes the boundaries of material design and control at the nano- and atomic-scale.

Associated Content

Supporting Information: Experimental details; Computational details; Phonon dispersions and energetics of $TaTe_3$ chains; Atomic and electronic structures of the single chain $TaTe_3$ configurations with different periodicities; Atomic and electronic structures of the three main phases of monolayer $TaTe_2$; Atomic structures of the studied $TaTe_2$ zigzag nanoribbons; Spatial visualization of the electron transfer between the carbon nanotube and $TaTe_2$ nanoribbon; Atomic structures of all distinct (meta)stable $TaTe_2$ monolayers found in this study; Electronic band structure and densities of states (DOS) of all distinct (meta)stable $TaTe_2$ monolayers found in this study

Acknowledgements

This work was primarily funded by the U.S. Department of Energy, Office of Science, Office of Basic Energy Sciences, Materials Sciences and Engineering Division, under Contract No. DE-AC02-05- CH11231 within the sp2-Bonded Materials Program (KC2207) which provided for synthesis of the chains, structural characterization, and theoretical modeling of relaxed structure of the NRs. The elemental mapping work was funded by the U.S. Department of Energy, Office of Science, Office of Basic Energy Sciences, Materials Sciences and Engineering Division, under Contract No. DE-AC02-05- CH11231 within the van der Waals Heterostructures Program (KCWF16). Work at the Molecular Foundry (TEAM 0.5 characterization) was supported by the Office of Science, Office of Basic Energy Sciences, of the U.S. Department of Energy under Contract No. DE-AC02-05-CH11231. Support was also provided by the National Science Foundation under Grant No. DMR-1807233 which provided

for preparation of opened nanotubes and Grant No. DMR 1926004 which provided for theoretical calculations of the electronic band structure of the materials. Computational resources were provided by the DOE at Lawrence Berkeley National Laboratory's NERSC facility and the NSF through XSEDE resources at NICS.

Author Contributions

S.S. and A.Z. conceived the idea; S.S. synthesized the materials; S.S., J.C., A.A., D.P., and A.C. performed electron microscopy data acquisition and analysis. M.D. and M.L.C. carried out density functional calculations. A. Z. and M.L.C. supervised the project; S.S., M.D., and AZ wrote the manuscript with input from all authors.

Competing interests

The authors declare no competing financial interest.

Additional Information

Correspondence and requests for materials should be addressed to A. Z.

Email: azettl@berkeley.edu

REFERENCES

[1] O. Lopez-Sanchez, D. Lembke, M. Kayci, A. Radenovic, and A. Kis, *Ultrasensitive Photodetectors Based on Monolayer MoS2*, Nature Nanotechnology **8**, 497 (2013).

[2] J. Guo, F. Li, Y. Sun, X. Zhang, and L. Tang, *Oxygen-Incorporated MoS<inf>2</Inf> Ultrathin Nanosheets Grown on Graphene for Efficient Electrochemical Hydrogen Evolution*, Journal of Power Sources **291**, 195 (2015).

[3] J. O. Island, A. J. Molina-Mendoza, M. Barawi, R. Biele, E. Flores, J. M. Clamagirand, J. R. Ares, C. Sánchez, H. S. J. Van Der Zant, R. D'Agosta, I. J. Ferrer, and A. Castellanos-Gomez, *Electronics and Optoelectronics of Quasi-1D Layered Transition Metal Trichalcogenides*, 2D Materials **4**, 022003 (2017).

[4] RadisavljevicB, RadenovicA, BrivioJ, GiacomettiV, KisA, B. Radisavljevic, A. Radenovic, J. Brivio, V. Giacometti, and A. Kis, *Single-Layer MoS2 Transistors*, Nat Nano **6**, 147 (2011).

[5] Y. Li, Y. Li, C. M. Araujo, W. Luo, and R. Ahuja, *Single-Layer MoS2 as Efficient Photocatalyst*, Catalysis Science and Technology **3**, 2214 (2012).

[6] Q. H. Wang, K. Kalantar-Zadeh, A. Kis, J. N. Coleman, and M. S. Strano, *Electronics and Optoelectronics of Two-Dimensional Transition Metal Dichalcogenides*, Nature Nanotechnology **7**, 699 (2012).

[7] T. Yang, H. Lin, K. P. Loh, and B. Jia, *Fundamental Transport Mechanisms and Advancements of Graphene Oxide Membranes for Molecular Separation*, Chemistry of Materials **31**, 1829 (2019).

[8] S. B. Basuvalingam, Y. Zhang, M. A. Bloodgood, R. H. Godiksen, A. G. Curto, J. P. Hofmann, M. A. Verheijen, W. M. M. Kessels, and A. A. Bol, *Low-Temperature Phase-Controlled Synthesis of Titanium Di- And Tri-Sulfide by Atomic Layer Deposition*, Chemistry of Materials **31**, 9354 (2019).

[9] C. H. Revolinsky, E., Brown, B. E., Beernsten, D. J., and Armitage, *The Selenide and Telluride Systems of Niobium and Tantalum*, Journal of the Less Common Metals **8**, 63 (1965).

[10] A. Brattas, Leif; Kjekshus, *The Non-Metal Rich Region of the Hf-Te System*, Acta Chemica Scandinavica **25**, 2783 (1971).

[11] L. H. Brixner, *Preparation and Properties of the Single Crystalline AB2-Type Selenides and Tellurides of Niobium, Tantalum, Molybdenum and Tungsten*, Journal of Inorganic and Nuclear Chemistry **24**, 257 (1962).

[12] J. Dai, M. Li, and X. C. Zeng, *Group IVB Transition Metal Trichalcogenides: A New Class of 2D Layered Materials beyond Graphene*, Wiley Interdisciplinary Reviews: Computational Molecular Science **6**, 211 (2016).

[13] S. Manzeli, D. Ovchinnikov, D. Pasquier, O. V. Yazyev, and A. Kis, *2D Transition Metal Dichalcogenides*, Nature Reviews Materials **2**, 17033 (2017).

[14] A. Splendiani, L. Sun, Y. Zhang, T. Li, J. Kim, C. Y. Chim, G. Galli, and F. Wang, *Emerging Photoluminescence in Monolayer MoS_2*, Nano Letters **10**, 1271 (2010).

[15] S. Meyer, T. Pham, S. Oh, P. Ercius, C. Kisielowski, M. L. Cohen, and A. Zettl, *Metal-Insulator Transition in Quasi-One-Dimensional $HfTe_3$ in the Few-Chain Limit*, Physical Review B **100**, 041403 (2019).

[16] M. Nagata, S. Shukla, Y. Nakanishi, Z. Liu, Y. C. Lin, T. Shiga, Y. Nakamura, T. Koyama, H. Kishida, T. Inoue, N. Kanda, S. Ohno, Y. Sakagawa, K. Suenaga, and H. Shinohara, *Isolation of Single-Wired Transition-Metal Monochalcogenides by Carbon Nanotubes*, Nano Letters **19**, 4845 (2019).

[17] T. Pham, S. Oh, S. Stonemeyer, B. Shevitski, J. D. Cain, C. Song, P. Ercius, M. L. Cohen, and A. Zettl, *Emergence of Topologically Nontrivial Spin-Polarized States in a Segmented Linear Chain*, Physical Review Letters **124**, 20 (2020).

[18] T. Pham, S. Oh, P. Stetz, S. Onishi, C. Kisielowski, M. L. Cohen, and A. Zettl, *Torsional Instability in the Single-Chain Limit of a Transition Metal Trichalcogenide*, Science **361**, 263 (2018).

[19] J.-J. Zhang, J. Guan, S. Dong, and B. I. Yakobson, *Room-Temperature Ferroelectricity in Group-IV Metal Chalcogenide Nanowires*, J. Am. Chem. Soc. **141**, 15040 (2019).

[20] R. J. Kashtiban, M. G. Burdanova, A. Vasylenko, J. Wynn, P. V. C. Medeiros, Q. Ramasse, A. J. Morris, D. Quigley, J. Lloyd-Hughes, and J. Sloan, *Linear and Helical Cesium Iodide Atomic Chains in Ultranarrow Single-Walled Carbon Nanotubes: Impact on Optical Properties*, ACS Nano **15**, 13389 (2021).

[21] J. D. Cain, S. Oh, A. Azizi, S. Stonemeyer, M. Dogan, M. Thiel, P. Ercius, M. L. Cohen, and A. Zettl, *Ultranarrow TaS2 Nanoribbons*, Nano Letters **21**, 3211 (2021).

[22] Z. Wang, H. Li, Z. Liu, Z. Shi, J. Lu, K. Suenaga, S. K. Joung, T. Okazaki, Z. Gu, J. Zhou, Z. Gao, G. Li, S. Sanvito, E. Wang, and S. Iijima, *Mixed Low-Dimensional Nanomaterial: 2D Ultranarrow MoS_2 Inorganic Nanoribbons Encapsulated in Quasi-1D Carbon Nanotubes*, Journal of the American Chemical Society **132**, 13840 (2010).

[23] A. Azizi, M. Dogan, J. D. Cain, K. Lee, X. Yu, W. Shi, E. C. Glazer, M. L. Cohen, and A. Zettl, *Experimental and Theoretical Study of Possible Collective Electronic States in Exfoliable Re-Doped NbS2*, ACS Nano **15**, 18297 (2021).

[24] P. M. Pelz, H. G. Brown, S. Stonemeyer, S. D. Findlay, A. Zettl, P. Ercius, Y. Zhang, J. Ciston, M. C. Scott, and C. Ophus, *Phase-Contrast Imaging of Multiply-Scattering Extended Objects at Atomic Resolution by Reconstruction of the Scattering Matrix*, Physical Review Research **3**, 1 (2021).

[25] X. Zhao, J. Qiao, S. M. Chan, J. Li, J. Dan, S. Ning, W. Zhou, S. Y. Quek, S. J. Pennycook, and K. P. Loh, *Unveiling Atomic-Scale Moiré Features and Atomic Reconstructions in High-Angle Commensurately Twisted Transition Metal Dichalcogenide Homobilayers*, Nano Letters **21**, 3262 (2021).

[26] B. E. Brown, *The Crystal Structures of $NbTe_2$ and $TaTe_2$*, Acta Crystallographica **20**, 264 (1966).

[27] J. Feng, A. Tan, S. Wagner, J. Liu, Z. Mao, X. Ke, and P. Zhang, *Charge Modulation and Structural Transformation in TaTe2 Studied by Scanning Tunneling Microscopy/Spectroscopy*, Applied Physics Letters **109**, 021901 (2016).

[28] Y. Liu, D. F. Shao, L. J. Li, W. J. Lu, X. D. Zhu, P. Tong, R. C. Xiao, L. S. Ling, C. Y. Xi, L. Pi, H. F. Tian, H. X. Yang, J. Q. Li, W. H. Song, X. B. Zhu, and Y. P. Sun, *Nature of Charge Density Waves and Superconductivity in 1T-TaSe2-XTex*, Physical Review B **94**, 045131 (2016).

[29] L. L. Wei, S. S. Sun, K. Sun, Y. Liu, D. F. Shao, W. J. Lu, Y. P. Sun, H. F. Tian, and H. X. Yang, *Charge Density Wave States and Structural Transition in Layered Chalcogenide $TaSe_{2-x}Te_x$*, Chinese Physics Letters **34**, 1 (2017).
[30] I. Kar, K. Dolui, L. Harnagea, Y. Kushnirenko, G. Shipunov, N. C. Plumb, M. Shi, B. Büchner, and S. Thirupathaiah, *Experimental Evidence of a Stable 2 H Phase on the Surface of Layered 1 T'-TaTe2*, Journal of Physical Chemistry C **125**, 1150 (2021).
[31] D. C. Miller, S. D. Mahanti, and P. M. Duxbury, *Charge Density Wave States in Tantalum Dichalcogenides*, Physical Review B **97**, 045133 (2018).
[32] S. Stonemeyer, J. D. Cain, S. Oh, A. Azizi, M. Elasha, M. Thiel, C. Song, P. Ercius, M. L. Cohen, and A. Zettl, *Stabilization of $NbTe_3$, VTe_3, and $TiTe_3$ via Nanotube Encapsulation*, Journal of the American Chemical Society **143**, 4563 (2020).
[33] B. I. Yakobson, C. J. Brabec, and J. Bernholc, *Nanomechanics of Carbon Tubes: Instabilities beyond Linear Response*, Phys. Rev. Lett. **76**, 2511 (1996).
[34] J. P. Lu, *Elastic Properties of Carbon Nanotubes and Nanoropes*, Physical Review Letters **79**, 1297 (1997).
[35] E. Hernández, C. Goze, P. Bernier, and A. Rubio, *Elastic Properties of C and BxCyNyComposite Nanotubes*, Physical Review Letters **80**, 4502 (1998).
[36] V. Popov, V. Van Doren, and M. Balkanski, *Elastic Properties of Single-Walled Carbon Nanotubes*, Physical Review B - Condensed Matter and Materials Physics **61**, 3078 (2000).
[37] K. N. Kudin, G. E. Scuseria, and B. I. Yakobson, *${\mathrm{C}}_{2}\mathrm{F},$ BN, and C Nanoshell Elasticity from Ab Initio Computations*, Phys. Rev. B **64**, 235406 (2001).
[38] S. Gupta, K. Dharamvir, and V. K. Jindal, *Elastic Moduli of Single-Walled Carbon Nanotubes and Their Ropes*, Physical Review B - Condensed Matter and Materials Physics **72**, 165428 (2005).

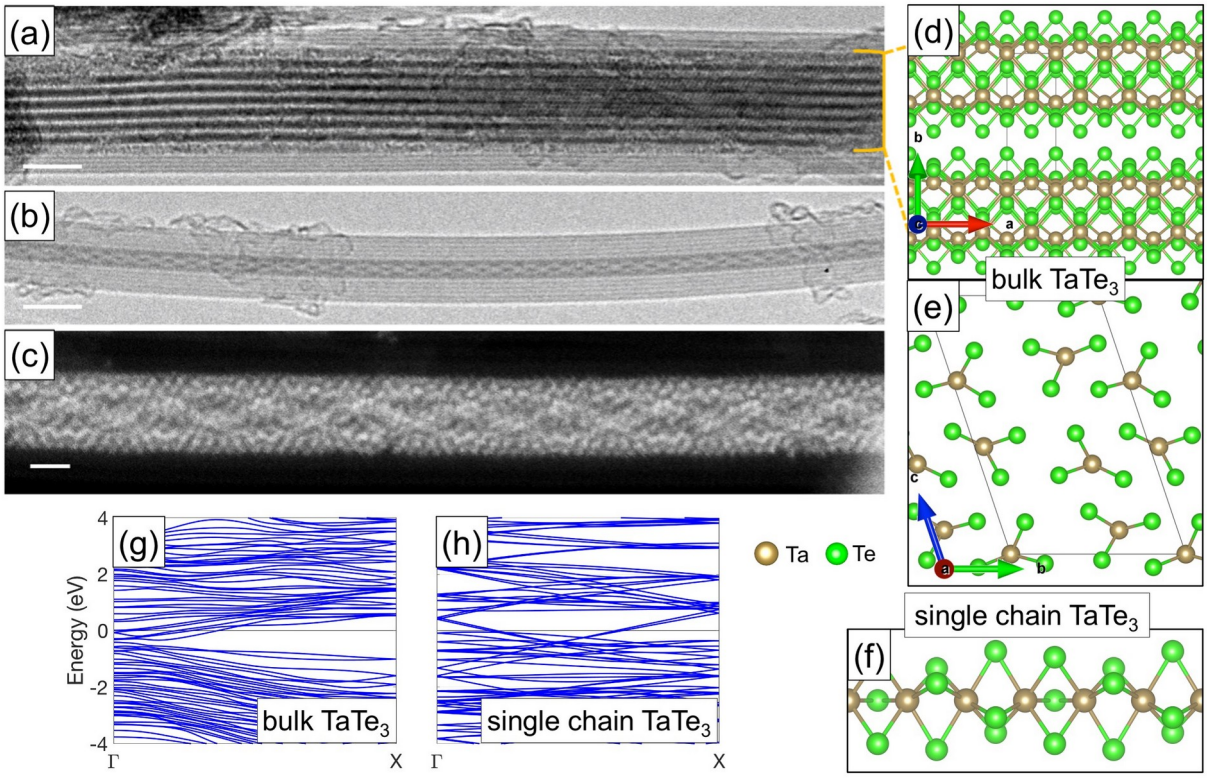

Figure 1. Electron microscopy images of encapsulated $TaTe_3$ chains. (a) TEM image of multi-chain $TaTe_3$ encapsulated in a 9.4 nm inner diameter CNT. The numerous parallel chains essentially constitute "bulk" $TaTe_3$. (b) and (c) TEM and STEM images of spiraling few-chain $TaTe_3$, encapsulated in 2.2 nm and 2.6 nm inner diameter CNT, respectively. Scale bars measure (a,b) 5 nm and (c) 1 nm. (d,e) Atomic model for bulk $TaTe_3$, with a side view (d) and end view (e) of the trigonal prismatic chains. (f) Atomic model for single chain $TaTe_3$. Ta and Te atoms are represented by gold and green spheres, respectively. (g,h) Electronic band structure of bulk (g) and single chain (h) $TaTe_3$, computed with spin–orbit coupling. The zero of the energy is set to the Fermi level.

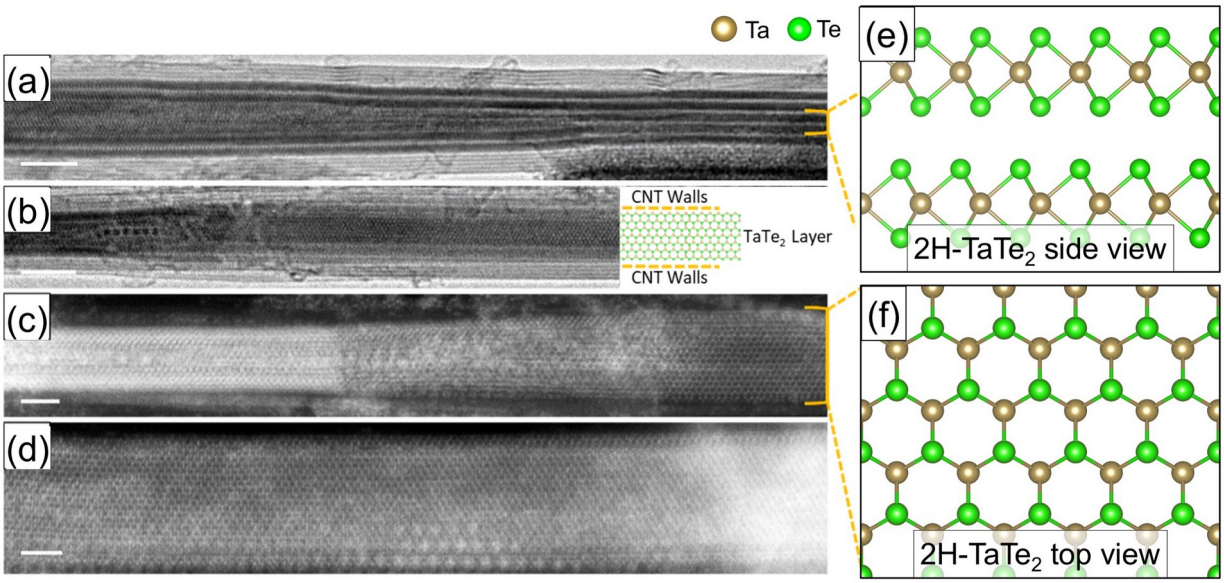

Figure 2. Electron microscopy images of encapsulated $TaTe_2$ Nanoribbons. (a) TEM image of a curling, multilayer NR. Layer edges are clearly visible on the right-hand side of the image. (b) TEM image of a monolayer NR. (c) STEM image of a monolayer NR. (d) STEM image of the basal plane of a flat monolayer NR. Scale bars measure (a,b) 5 nm and (c,d) 2 nm. (e) Atomic model of the edge view of 2H-$TaTe_2$, which should approximate the structure of the layer edges in (a). (f) Atomic model of the top view of 1H-$TaTe_2$, which corresponds to the structure in (c). Ta and Te atoms are represented by gold and green spheres, respectively.

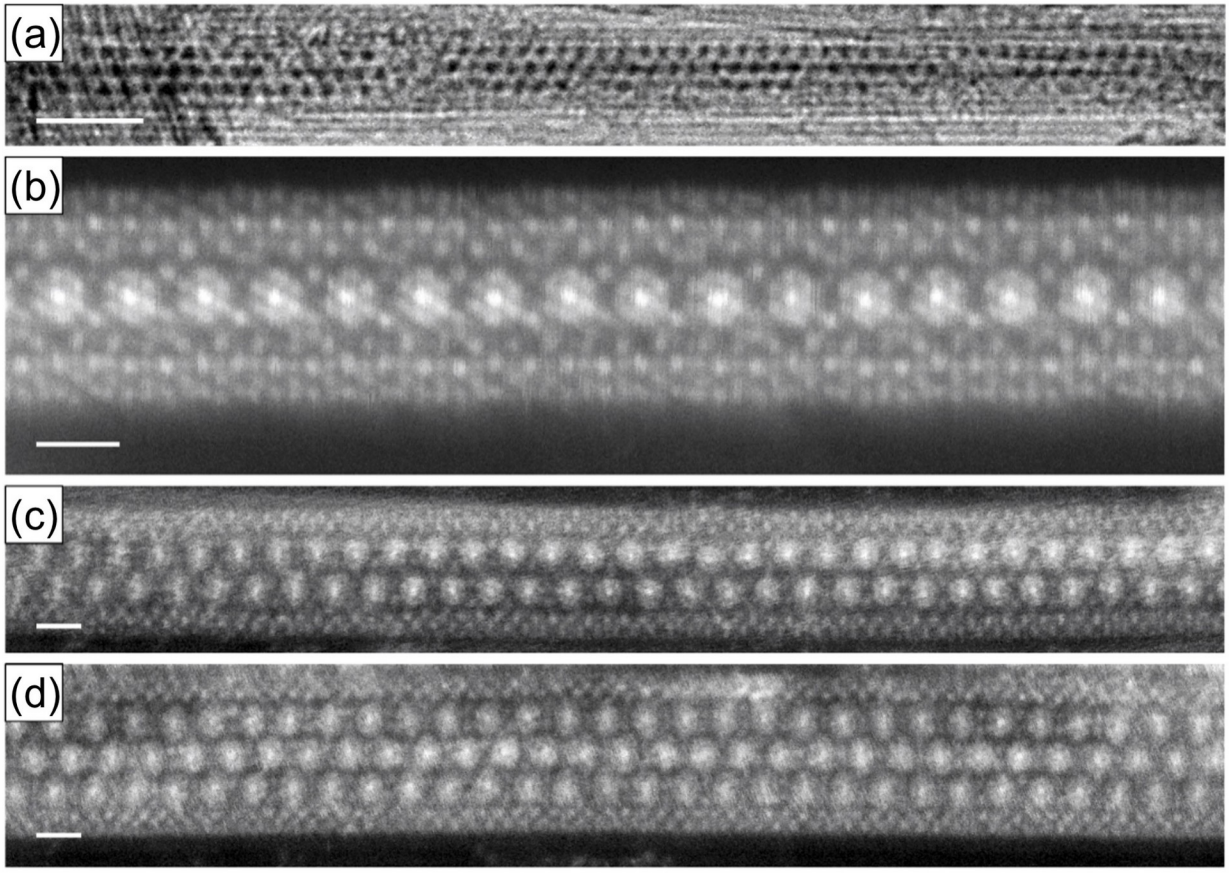

Figure 3. Electron microscopy images of the encapsulated moiré-like TaTe species. (a) TEM image of the moiré-like structure about 3 patterns wide. (b,c,d) STEM images of the moiré-like structure from increasing widths, from a single pattern, double pattern, and triple pattern wide, respectively. Scale bars measure (a) 5 nm and (b,c,d) 1 nm.

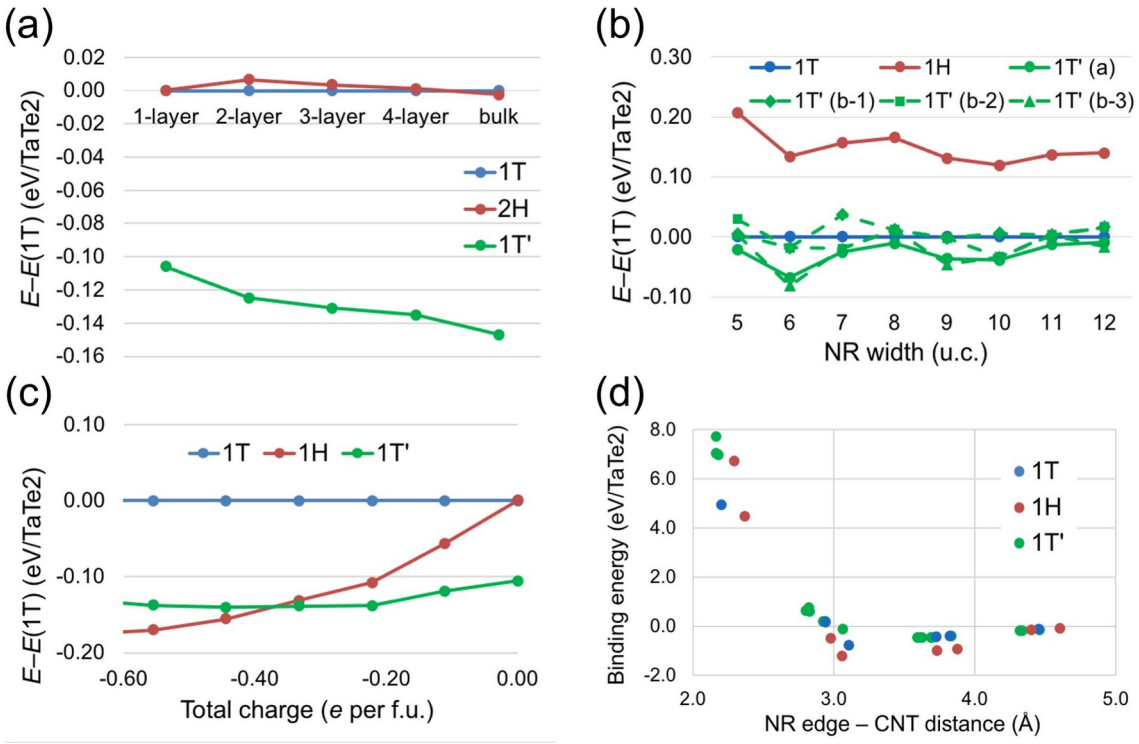

Figure 4. Energetic comparisons between the three main phases of $TaTe_2$. (a,b,c) Total energy with respect to 1T examined as a factor of (a) number of layers, (b) nanoribbon (NR) width, and (c) total charge. (d) For NRs encapsulated in carbon nanotubes (CNTs), the binding energy of each $TaTe_2$ configuration as a function of distance between the NR edge and the CNT inner walls.

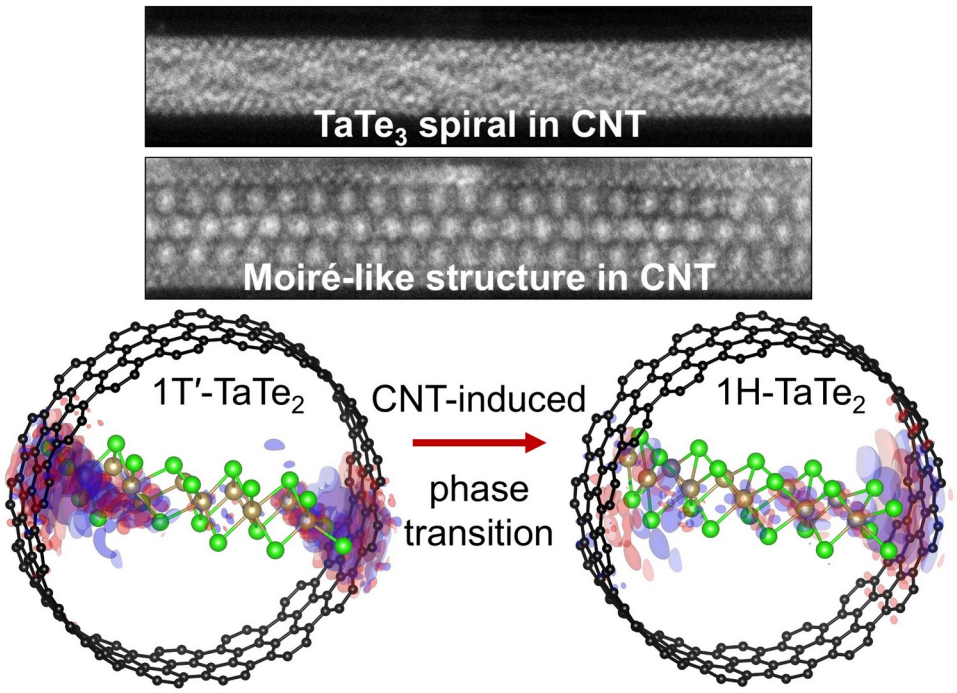
TaTe3 spiral in CNT
Moiré-like structure in CNT
1T′-TaTe2
CNT-induced
phase
transition
1H-TaTe2

ToC Graphic